Electronic Supplementary Material (ESI) for Lab on a Chip.


# Supporting information

## Out-of-plane faradaic ion concentration polarization: stable focusing of charged analytes at a three-dimensional porous electrode.

Beatrise Berzina,[a] Sungu Kim,[a,b] Umesha Peramune,[a] Kumar Saurabh,[b] Baskar Ganapathysubramanian,[b] Robbyn K. Anand.[a]*

[a]The Department of Chemistry, Iowa State University, 2415 Osborn Drive, 1605 Gilman Hall, Ames, Iowa 50011-1021, United States.

[b]The Department of Mechanical Engineering, Iowa State University, 2043 Black Engineering, 2529 Union Drive, Ames, Iowa 50011-2030, United States.

This supporting information includes detailed information and procedures regarding 1) device designs and fabrication, 2) verification of the mechanism of fICP, 3) assessment of the projected area and growth rate of the IDZ, 4) collection of current transients and current-voltage curves (CVCs), 5) measurement of the onset potential of water reduction on several distinct electrode materials, 6) electrokinetic enrichment of charged species, 7) scalability of the device, and 8) computational method for charged species transport simulation.

**Chemicals**. The charged fluorophore, $BODIPY^{2-}$ (4,4-fluoro-1,3,5,7,8-pentamethyl-4-bora-3a,4a-diaza-S-indacene-2,6-disulfonic acid, disodium salt) and Texas Red dye-linked bovine serum albumin (Texas Red BSA) were obtained from Invitrogen (Carlsbad, CA). All other solutions were prepared using reagent grade chemicals (Fisher Scientific, Waltham, MA) and diluted with double deionized water (18.2 MΩ·cm, Sartorius Arium Pro, Göttingen, Germany) to desired concentration. Poly(dimethylsiloxane) (Sylgard 184 elastomer kit, Dow Corning Corp., Midland, MI) was used for device fabrication. Polystyrene carboxylate beads (diameter, $d = 20$ μm) were purchased from Polysciences Inc. (Warrington, PA). Conductive silver-coated hollow glass microspheres ($d$ = 10-20 μm, 0.67 g/cc) were purchased from Cospheric (Santa Barbara, CA). Gold-coated glass slides with a Cr adhesion layer (1” x 3” x 0.40”; 50 Å Cr, 1,000 Å Au)

were purchased from Evaporated Metal Films (Ithaca, NY) and were used for fabrication of patterned thin film electrodes.

**Fluorescence imaging and data processing**. All fluorescence measurements were obtained using an Eclipse Ti-S inverted fluorescence microscope (Nikon Industries, New York, NY) equipped with a digital camera (Orca Flash 4.0, Hamamatsu Corp., Bridgewater, NJ). All images were processed using NIS-Elements 4.6 software (Nikon) and ImageJ (NIH). Fluorescence intensities used for quantitative comparison of IDZ growth and for calculation of EF were background subtracted and processed using MATLAB (The MathWorks Inc. Natick, MA) and NIS-Elements 4.6 software.

Fluorescence intensities used for enrichment factor (EF) calculations were background subtracted. EF was calculated by comparing the brightest region of the enriched plug (average of 10 contiguous pixels with the highest intensity) to the initial fluorescence intensity prior to enrichment. An important point is that the EF of an enriched plug confined to the PSC bead bed was calculated by comparing to the initial intensity measured within the bed. The EF calculation was carried out using the following equation:

$$EF = \frac{I_{av} - I_b}{I_o - I_b} \qquad \text{eq. S1}$$

where $I_{av}$ is the average of the 10 highest contiguous pixel intensities within the enriched plug, $I_b$ background intensity, $I_0$ initial fluorescence intensity, obtained prior to enrichment.

**Device design and fabrication**. The microfluidic devices were fabricated using standard photolithographic processes.[1] Channel molds were patterned using negative photoresist (SU-8 2050, Microchem Corp., Westborough, MD) coated on a Si substrate followed by casting with PDMS. **Scheme S1** depicts the device design and setup all three device architectures. The main channel was 40.0 µm tall, 11.0 mm long, and 1.48 mm wide. The width of the bead bed was 0.30 mm, and there were 10.0 µm gaps between the posts (20 µm wide) used to retain the bead. Auxiliary channels used for packing the bead beds were 0.20 mm wide and 2.5 mm long. A 1.0 mm diameter biopsy punch was used to create the inlet

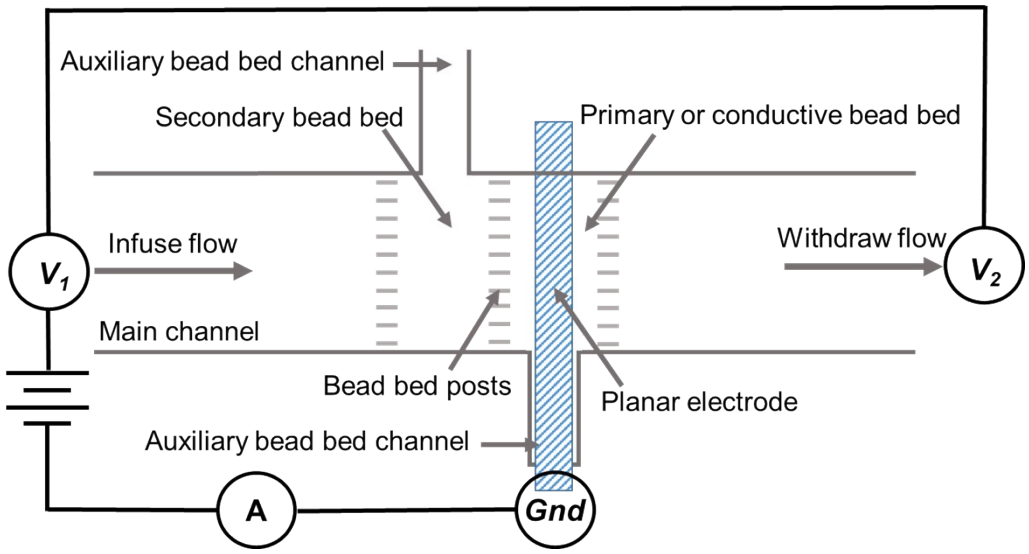


**Scheme S1**. Schematic representation of the device design near the center of the main channel including the planar electrode, bead beds, and the auxiliary channels employed to pack the beads. The channel segments leading to the inlet and outlet are not depicted. The voltage bias was applied between the driving electrodes (indicated by $V_1$ and $V_2$) and the wire lead connected to the planar electrode (*Gnd*). The sample solution is infused into the inlet (at left) and withdrawn from the outlet (at right).

and outlet reservoirs of the main channel, and the inlet of the auxiliary channels for bead bed packing.

Au electrodes were microfabricated on glass slides using a previously published method.[2] The patterned Au electrode width was 0.2 mm and it was centered at the midpoint of the main channel, underneath the primary (conductive) bead bed. This electrode was sufficiently long to extend out from under the PDMS monolith to make contact to a wire lead. The PDMS layer and glass slide with patterned Au film were treated in an air plasma (PDC-001, Harrick Plasma, Ithaca, NY) for 60 s and then placed in contact to bond. To enhance the bond strength, the device was incubated at 65°C for at least 18 h.

A suspension of the conductive Ag-coated beads in DDI (5.0 µL, w/v = 22 mg $mL^{-1}$) was packed into the primary bead bed by pipetting them into the inlet and applying pressure. When a secondary bead

bed was used, a suspension of polystyrene carboxylate (PSC) beads (10 μL, 10 v/v% in DDI) was packed into the inlet of the auxiliary channel of the secondary bead bed using the same method. The inlets of these auxiliary channels were then sealed by adding a drop (approx. 40 μL) of PDMS, which was subsequently cured by incubating the device at 65ºC for 3 h. Devices were filled with buffer at concentration matching that utilized in subsequent experiments prior to use. The driving electrodes were comprised of 1 mm O.D. stainless steel tubing that connected the inlet and outlet of each device to PTFE tubing. An identical device design with increased width of the main channel (3.0 mm), used to demonstrate scalability of out-of-plane fICP devices. The dimensions for both devices are summarized in **Table S1**.

**Table S1**. Device dimensions.

| Device design | Channel width, mm | Channel length, mm | Channel height, μm | Primary or conductive bead bed width, μm | Secondary bead bed width, μm | Gap between bead bed posts, μm |
|---|---|---|---|---|---|---|
| 1 | 1.48 | 11.0 | $40.0 \pm 0.5$ | 300 | 500 | 10 |
| 2 | 3.00 | 11.0 | $38.0 \pm 0.5$ | 300 | 500 | 10 |

**Verification of IDZ generation by the fICP mechanism**. In these experiments, the microchannel was rinsed for 20 min with Tris buffer before filling the inlet reservoir with 10.0 μL of running solution (see the following paragraph), spiked with 0.3 μM Texas Red BSA and 10 μM $BODIPY^{2-}$. Prior to use, devices were conditioned at 3.0 V for 5 min, at 200 nL $min^{-1}$. Flow was established using two syringe pumps (Pump 11 PicoPlus Elite, Harvard apparatus, Holliston, MA), each of which were equipped with a glass syringe (500 μL) connected to the device with 1.0 mm i.d. PTFE tubing. Importantly, uniform pressure driven flow was ensured by setting one pump to infuse into the inlet and the other pump to withdraw from the outlet reservoir. For IDZ growth measurements, the flow rate was decreased to 10 nL $min^{-1}$ allowing the flow to equilibrate for 10 min. Then, a potential between 0 V and 15.0 V was applied (6487 Picoammeter/Voltage source, Keithley, Cleveland, OH) and the current measured between the driving electrodes and Au microband. The current was recorded using ExceLINX (Keithley, Cleveland, OH) software. After each trial, the device was rinsed thoroughly with DDI, followed by running solution.

The running solutions tested include $KNO_3$ (10.0 mM, 1588 μS $cm^{-1}$), phosphate buffer (10.0 mM, pH 7.4, 2642 μS $cm^{-1}$), Tris buffer (10.0 mM, pH 8.3, 260 μS $cm^{-1}$), Tris buffer (40.0 mM, pH 8.3, 878 μS $cm^{-1}$), and Tris buffer (100.0 mM, pH 8.3, 2109 μS $cm^{-1}$). **Figure S1** depicts CVCs obtained for

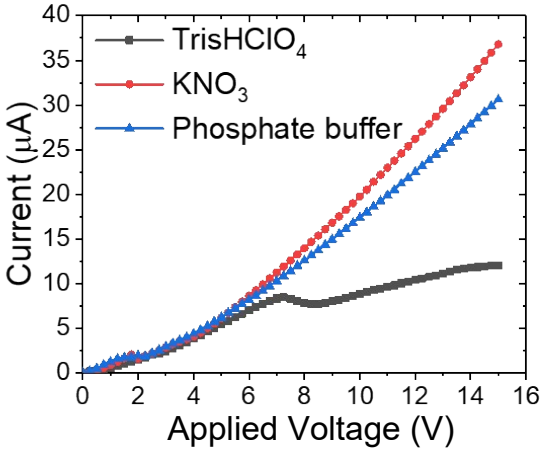


**Figure S1**. Graph demonstrating current-voltage curves for $TrisHClO_4$ (40.0 mM, black), $KNO_3$ (10.0mM, red) and phosphate (10.0 mM, blue) systems obtained using planar Au electrode device design. Voltage range 0-15.0 V, 0.25 V/step, 0.33s/step. Flow rate 10 nL $min^{-1}$ (infuse, withdraw).

three different solutions – Tris buffer (40.0 mM), $KNO_3$ (10.0 mM) and phosphate buffer (10.0 mM) using the planar Au device (no beads).

**Measurements of IDZ growth over time**. To facilitate filling, devices were evacuated in a vacuum desiccator for 20 min prior filling with Tris buffer. Prior to each experiment, the microchannels were rinsed for 20 min with Tris · $HClO_4$ buffer (40.0 mM, pH 8.3). The reservoirs were then filled with 40.0 mM Tris buffer with 10.0 μM $BODIPY^{2-}$. Prior to use, devices were conditioned for 5 min at 3.0 V under a flow rate of 200 nL $min^{-1}$. As described in the preceding section, uniform pressure driven flow was

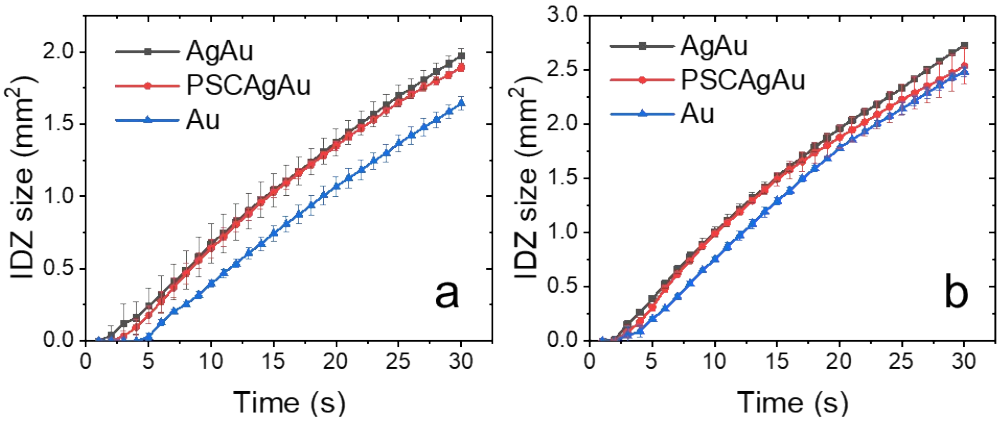


**Figure S2**. Plots of the projected area of the IDZ (IDZ size) as a function of time, obtained in planar Au (blue), Ag/Au (black), and PSC/Ag/Au (red) devices to which a voltage bias of a) 7.0 V and b) 10.0 V was applied. Flow rate, 10 nL $min^{-1}$. Solution composition: 10.0 $\mu$M $BODIPY^{2-}$ in 40.0 mM Tris buffer (pH 8.3).

ensured using infusion and withdrawal from the inlet and outlet reservoirs, respectively. Prior to IDZ growth measurements, the flow rate was decreased to 10 nL $min^{-1}$ and allowed to equilibrate for 10 min. To initiate fICP, a voltage bias of 5.0 V was applied and projected area of the IDZ was measured as the region over which the fluorescence intensity was $\leq$ 0.5-fold the initial fluorescence intensity. These measurements were repeated at a voltage bias of 7.0 and 10.0 V. Between each of these experiments, the device was refreshed by increasing the flow rate to 200 nL $min^{-1}$ for 20 s. The flow rate was once again decreased to 10 nL $min^{-1}$ and allowed to equilibrate for 10 min, before initiating the next experiment. All image sequences were processed using a MatLab program developed in-house. **Figure S2a-c** demonstrate IDZ growth over time using planar Au, Ag/Au and PSC/Ag/Au devices, repeated in three individual microfluidic devices for each of the device architectures. The plots of IDZ growth obtained at 5.0 V are shown in the main manuscript (**Figure 2**).

**Figure S3** shows IDZ growth in a device having two secondary (PSC) bead beds flanking the Ag/Au electrode. In this case, both boundaries of the IDZ are flat (have a straight edge). The ionic and fluidic resistance of this device are higher than for the PSC/Ag/Au case.

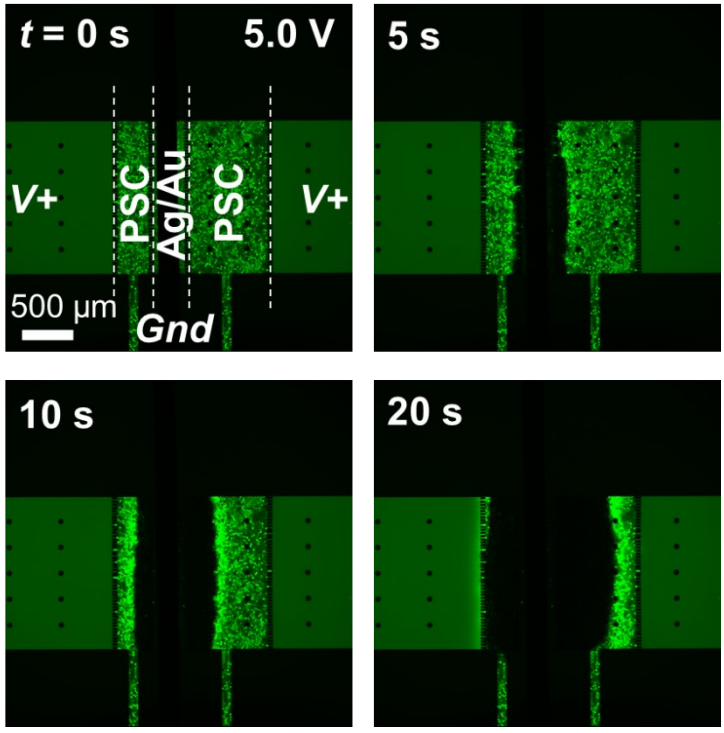


**Figure S3**. Fluorescence micrographs showing the IDZ at $t$ = 0, 5, 10, and 20 s in a device with two PSC bead beds flanking the Ag/Au electrode. Experimental conditions: 5.0 V, 10 nL $min^{-1}$, 10.0 $\mu$M $BODIPY^{2-}$ in 40.0 mM Tris buffer (pH 8.3).

**Measurement of current transients and CVCs**. To facilitate device filling, devices were evacuated in a vacuum desiccator for 20 min prior to filling with Tris buffer. Prior to each experiment, the microchannels were rinsed for 20 min with Tris buffer (40.0 mM, pH 8.3). The reservoirs were then filled with 10 μM $BODIPY^{2-}$ in 40.0 mM Tris buffer. **Scheme 2** (main manuscript) depicts the device designs used for measurement of current transients and CVCs. Prior to use, devices were conditioned at 3.0 V for 5 min, at 200 nL $min^{-1}$. Then, the flow rate was decreased to 10 nL $min^{-1}$ and allowed to equilibrate for 10 min. In between measurements, devices were refreshed by increasing the flow rate to 200 nL $min^{-1}$ for 20 s, and then decreasing to 10 nL $min^{-1}$ and allowing the flow to equilibrate for 10 min.

*Current transients*. Measurements proceeded as follows. First, the driving electrodes and Au planar microband were connected by power supply in series with a picoammeter (6487 Picoammeter/Voltage source, Keithley, Cleveland, OH). Second, 5.0 V were applied. The resulting current at the electrode was measured for 30 s using ExceLINX (Keithley, Cleveland, OH) software. Further, the device was rinsed according to the procedure described in the preceding paragraph before repeating at 7.0 and 10.0 V. **Figure S4a-b** shows current transients obtained in three individual devices for each architecture.

*Obtaining CVCs*. Evaluation of current-voltage relationship for each device architecture proceeded as follows. First, the driving electrodes and planar Au microband were connected by a power supply in series with a picoammeter. Second, a series of voltage steps from 0 V to 20.0 V were applied in 0.25 V increments at a rate of 0.33 s per step. The resulting current at the electrode was using ExceLINX (Keithley, Cleveland, OH) software. Between each CVC, the device was rinsed according to the procedure described in the preceding paragraphs. **Figure 3** (main text) demonstrates CVCs obtained in three individual devices for each of the three device architectures.

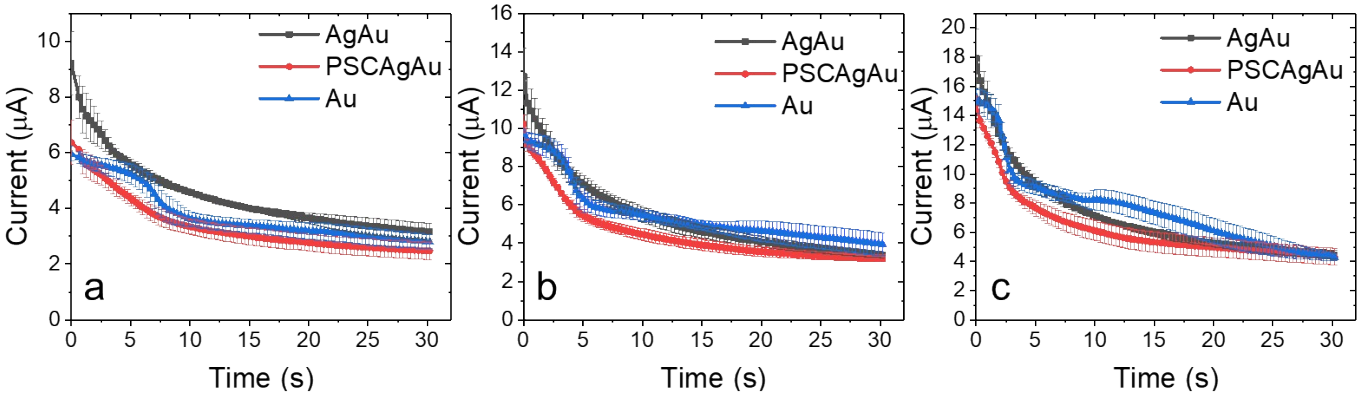


**Figure S4**. Graphs demonstrating current transients for planar Au (blue), PSC/Ag/Au (red), and Ag/Au (black) devices. Measurements taken at a) 5.0 V, b) 7.0 and c) 10.0 V, Flow rate 10 nL $min^{-1}$.

**Evaluation of fICP with a bed of PSC microspheres overlying the planar Au electrode.** To clarify the role of the 3D electrode comprising conductive Ag microbeads in fICP, the formation of an IDZ, current transient, and CVC were evaluated in a control case – a device having a bed of PSC microbeads overlying the Au planar microband. The experimental conditions for each experiment type was unchanged from that utilized for the other device architectures. **Figure S5** shows the results of these experiments.

**Figure S5a** is a series of fluorescence micrographs showing the formation of an IDZ under slow continuous flow (left to right, 10 nL $min^{-1}$). The boundary of the IDZ exhibits smaller electroconvective vortices than that observed at the planar Au electrode but was less symmetrical than that observed in either the Ag/Au or PSC/Ag/Au devices (compare to **Figure 2a**, main text).

**Figure S5b** is a plot of the projected area of the IDZ as a function of time. IDZ growth in this PSC/Au device had an intermediate onset time (3 s) to that observed in the Ag/Au and Au devices. We attribute the earlier IDZ propagation (than at the Au planar electrode alone) to the small interstitial volume (between PSC microbeads) that must be depleted for the IDZ to reach the "ceiling" of the microchannel.

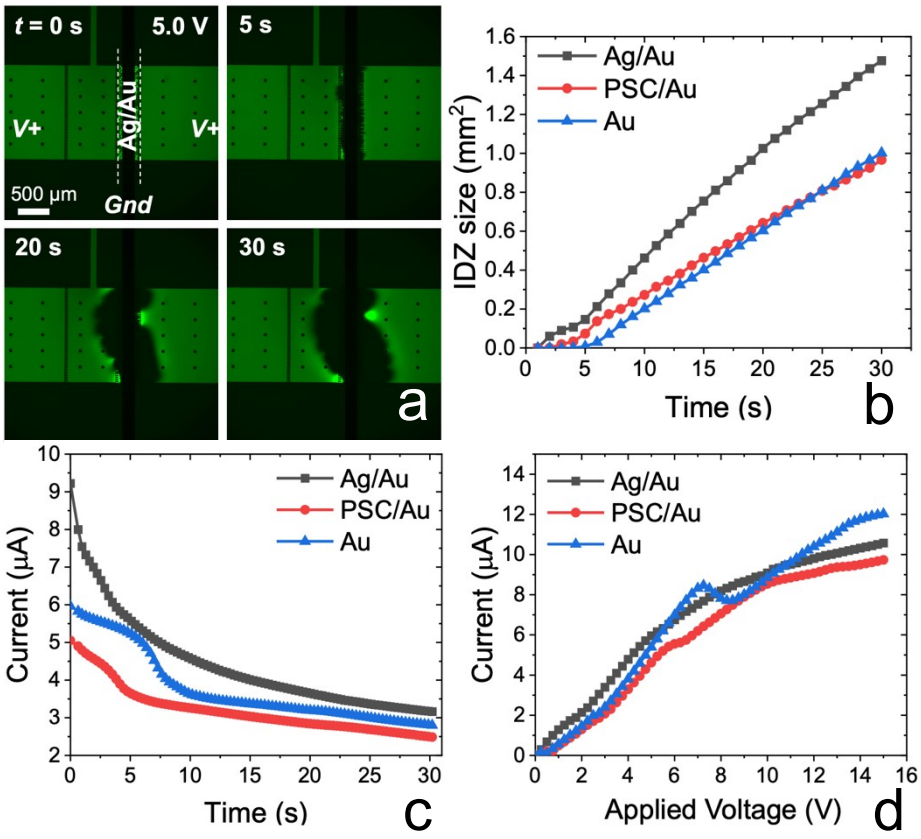


**Figure S5**. The results of fICP in the PSC/Au device (control case) including a) a series of fluorescence micrographs showing the propagation of the IDZ, b) plot of the projected IDZ area as function of time, c) current transients obtained, and d) CVCs. In (a-c), $V^{+}$ = 5.0 V initiated at $t$ = 0. For (c,d), results obtained for Au and Ag/Au device included for comparison.

The later onset of propagation relative to the Ag/Au device can be attributed to the lower current in the PSC/Au device, which also exhibited a slower rate of IDZ growth (shallow slope) than any other device architecture. This delayed onset of propagation and slow rate of IDZ growth is attributed to the lower current (lower rate of ion consumption) in the presence of insulating beads packed on top of the electrode.

**Figure S5c** is a current transient obtained for the PSC/Au control. The current is lower at all times relative to the other device architectures and exhibits a stepwise decay at $t$ = 3 s, which corresponds with the observed onset of outward IDZ propagations from the electrode (**Figure S5b**). The current observed in this PSC/Au device was also lower than other device types under a voltage sweep (CVC, **Figure S5d**). A key point is that, while the limiting regime is truncated by the PSC microbeads (relative to the Au planar electrode alone), it is not completely absent as is the case in the Ag/Au device. This result indicates that the metallic microbeads play an important role in supporting mass transport of ions to the electrode surface. When taken in the context of the simulation results, this role of Ag microbeads can be attributed to the nucleation of small, rapid vortices at their surfaces.

**Measurement of the potential of water reduction at four electrode materials.** A voltammetric study was performed to determine the onset potential for water reduction using four different working electrode materials: Pt disk ($d$ = 3.0 mm), Au disk ($d$ = 3.0 mm), and glassy carbon (GCE) disk ($d$ = 3.0 mm) microelectrodes and a Ag wire (17 mm long, $d$ = 1.0 mm) immersed in 40.0 mM Tris · $HClO_4$ buffer (pH 8.3, 878 μS $cm^{-1}$).

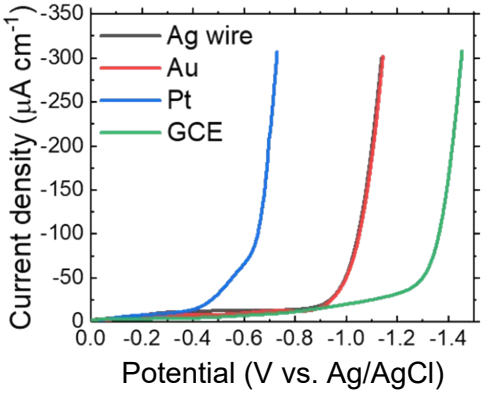


**Figure S6**. Linear sweep voltammogram obtained for water reduction in 40.0 mM Tris · $HClO_4$ buffer employing various working electrode materials: Pt (blue), glassy carbon (GCE, green), Au (red), and Ag (black) in 3-electrode cell with a Ag/AgCl reference electrode and a Pt mesh counter electrode. Sweep rate, 50 mV $s^{-1}$.

*Voltammetric study*. Measurements were recorded using a Pine WaveDriver 20 Bipotentiostat/ Galvanostat (Pine Instruments, Durham, NC, US). The electrochemical cell consisted of the driving electrode (Pt, Au, GCE or Ag wire), Ag/AgCl reference electrode and Pt mesh auxiliary electrode. Prior to experiments, electrodes were polished using a published method[3] and dried with a stream of $N_2$ gas. To further condition the Au microelectrode, cyclic voltammetric scans (60 scans, 0.50 mV $s^{-1}$, -0.40 V to 1.75 V vs. Ag/AgCl reference) were performed in a cell containing 0.5 M $H_2SO_4$ solution.

*Onset of water reduction at each working electrode material*. 40.0 mM Tris · $HClO_4$ buffer (pH 8.3, 878 µS $cm^{-1}$) was sparged with $N_2$ for 15 min. Further, a $N_2$ stream was positioned above the solution while a linear sweep voltammogram was obtained to observe water reduction. The working electrode was then exchanged for the next material, and $N_2$ sparging was repeated for 5 min in between the trials. Three sequential voltammograms were recorded, at a sweep rate of 50 mV $s^{-1}$ for each of the working electrodes (**Figure S6**). Onset of water reduction was observed at -0.51 V (Pt), -0.97 V (Au), -0.97 V (Ag), and -1.31 V (GCE).

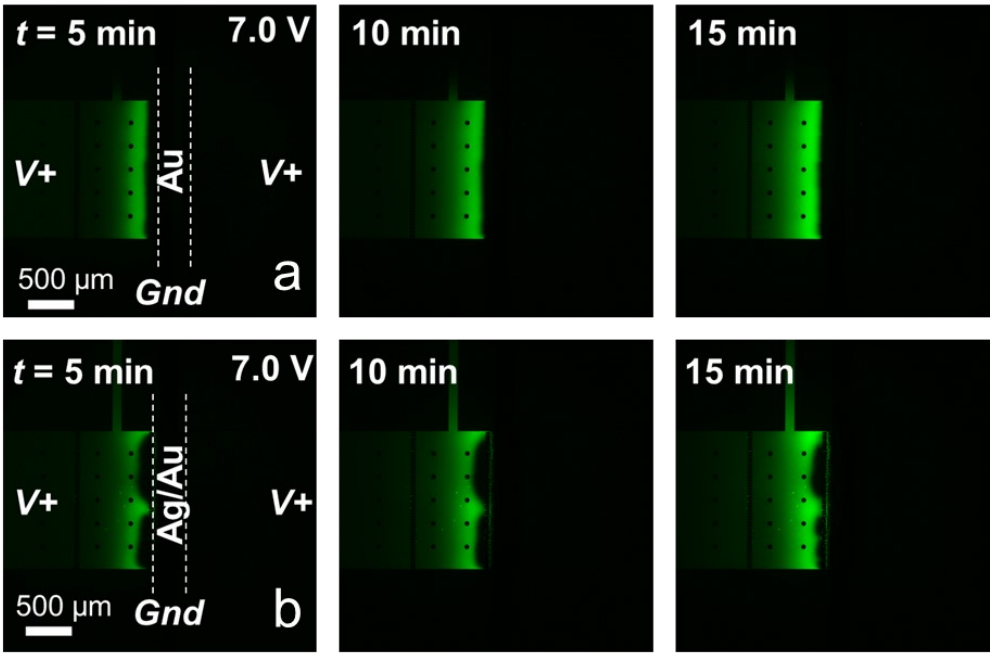


**Figure S7**. Fluorescence micrographs demonstrating enrichment of BODIPY2- (0.1 µM) in 20.0 mM TrisHClO4 buffer at various time points using a) Au and b) Ag/Au electrode. Experimental conditions: 7.0 V, 100 nL min -1 (infuse, withdraw).

**Charged species electrokinetic enrichment by fICP.** To facilitate device filling, devices were evacuated in a vacuum desiccator for 20 min prior to filling with Tris buffer. Prior to experiments, the microchannels were rinsed for 20 min with Tris · $HClO_4$ buffer (20.0 mM, pH 8.3). The reservoirs were then filled with 0.1 µM $BODIPY^{2-}$ in 20.0 mM $TrisHClO_4$. Next, devices were conditioned at 3.0 V for 5 min, at a flow rate of 200 nL $min^{-1}$. The flow rate was then decreased to 100 nL $min^{-1}$ and allowed to equilibrate for 10 min. Finally, a driving voltage of 7.0 V was applied. Fluorescence micrographs were taken every 30 s for 15 min after initiation of the driving voltage. Fluorescence intensity used for EF calculations was background subtracted. The mean of the 10 pixels with the highest intensity was used to calculate EF. **Figure S7a,b** are two series of fluorescence micrographs obtained at $t$ = 5, 10, and 15 min after applying $V$+ = 7.0 V in a a) planar Au and b) Ag/Au device.

**Scalability of the PSC/Ag/Au device**. To investigate the impact of device scale on concentration enrichment in the PSC/Ag/Au device, both the flow rate and channel width were doubled to 3.0 mm and 200 nL $min^{-1}$, respectively. The channel was filled with 0.1 $\mu$M $BODIPY^{2-}$ in 20.0 mM Tris buffer, and constant fluid flow was established. Then, $V$+ = 7.0 V was applied. **Figure S8a** is a fluorescence micrograph of the resulting enriched band of a tracer dye positioned within the PSC bead bed at $t$ = 450 s following initiation of the applied voltage. **Figure S8b** shows the evolution of the EF over this time

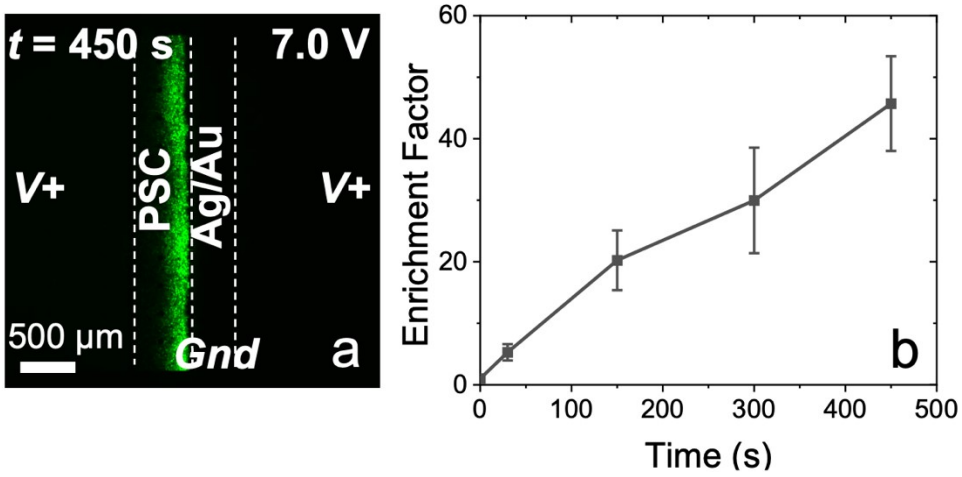


**Figure S8.** a) Fluorescence micrograph showing an enriched band of $BODIPY^{2-}$ at $t$ = 450 s after initiation of an applied voltage of $V$+ = 7.0 V in a PSC/Ag/Au device with a 3.0 mm channel width. b) Plot of EF as a function of time for the same experiment. Initial concentration, 0.1 $\mu$M $BODIPY^{2-}$ in 20.0 mM Tris buffer (grey line). Flow rate, 200 nL $min^{-1}$.

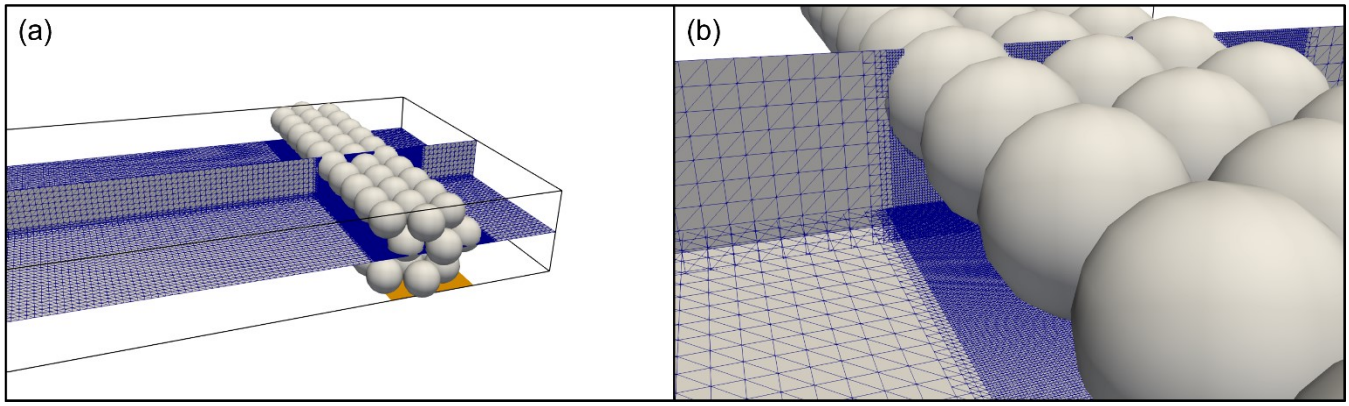


**Figure S9**. Problem geometry and octree-based adaptive mesh refinement. The yellow plate at the channel bottom represents Au electrode used in the experiment, and grey spheres for Ag particles. The mesh was refined near the Au and Ag surface to resolve the thin electric double layer.

period. The enrichment obtained over 450 s is a rate of 0.10-fold/s (20.0 mM Tris buffer), which is comparable to the rate (0.11-fold/s) observed in the narrower (1.48 mm-wide) device.

**Computational methods for charged species transport simulation**. To numerically solve coupled Navier-Stokes Poisson-Nernst-Planck equations, we used the previously described numerical framework with some updates for accuracy and stability.[4] In brief, finite element method (FEM) with variational multiscale method (VMS) was used to solve the coupled NS-PNP equations. A second order accurate linear basis function was used for spatial discretization. A second order time stepping methods, backward differentiation formula (BDF2), was deployed to achieve accurate and stable results. The problem geometry and mesh were generated using octree based adaptive mesh refinement ensuring computational efficiency and scalability.[5] **Table S2** states the boundary conditions for the numerical simulations. **Figure S9** shows the generated problem geometry and refined mesh. **Figure S10** shows the algorithm for solving the coupled NS-PNP system. At each timestep, we solve NS and PNP separately and iterate until the desired tolerance is achieved. A more detailed discussion is provided in Kim *et. al*. [4]

**Table S2.** Boundary condition details for the NS-PNP coupled numerical simulations.

| Solver | Position | Boundary Condition Type | Variable | Specification | Value |
|---|---|---|---|---|---|
| Navier-Stokes | Sphere, Top wall, Bottom wall | No - slip | u | Dirichlet | 0 |
| | | | v | Dirichlet | 0 |
| | | | w | Dirichlet | 0 |
| | | | p | Neumann | 0 |
| | Left wall | Inlet boundary condition | u | Dirichlet | Inlet velocity |
| | | | v | Dirichlet | 0 |
| | | | w | Dirichlet | 0 |
| | | | p | Neumann | 0 |
| | Right wall | Outlet boundary condition | u | Neumann | 0 |
| | | | v | Neumann | 0 |
| | | | w | Neumann | 0 |
| | | | p | Dirichlet | 0 |
| | Side walls | Symmetry boundary condition | u | Neumann | 0 |
| | | | v | Dirichlet | 0 |
| | | | w | Dirichlet | 0 |
| | | | p | Neumann | 0 |
| PNP | Sphere, Bottom electrode region | Electrode | $\emptyset$ | Dirichlet | 0 |
| | | | $c_1$ | Dirichlet | 0 |
| | | | $c_2$ | Neumann | 0 |
| | Left wall | Inlet boundary condition | $\emptyset$ | Dirichlet | $V^+$ |
| | | | $c_1$ | Dirichlet | 1 |
| | | | $c_2$ | Neumann | 1 |
| | Right wall | Outlet Boundary condition | $\emptyset$ | Neumann | 0 |
| | | | $c_1$ | Neumann | 0 |
| | | | $c_2$ | Neumann | 0 |
| | Side walls, Bottom walls except electrode region | Symmetry boundary condition | $\emptyset$ | Neumann | 0 |
| | | | $c_1$ | Neumann | 0 |
| | | | $c_2$ | Neumann | 0 |

The numerical method was solved for the background electrolyte in $H_2O$ at 25 °C. The viscosity and density of $H_2O$ was $1.00 \times 10^3$ Pa·s and $9.98 \times 10^2$ kg/m$^3$, respectively. The diffusivity of the cation and anion were assumed to be equal, at $3.0 \times 10^{-9}$ m$^2$/s. The relative permittivity was 80. For the given channel height of 40 μm and initial concentration of 10 mM, the thickness of the non-dimensional Debye layer ($\Lambda$ in equation (1) and (2)) was $7.61 \times 10^{-5}$. The Schmidt number, $Sc$ in equation (1), was $3.00 \times 10^{-3}$, and the electrohydrodynamic coupling constant, $\kappa$ in equation (1), was 0.1489.

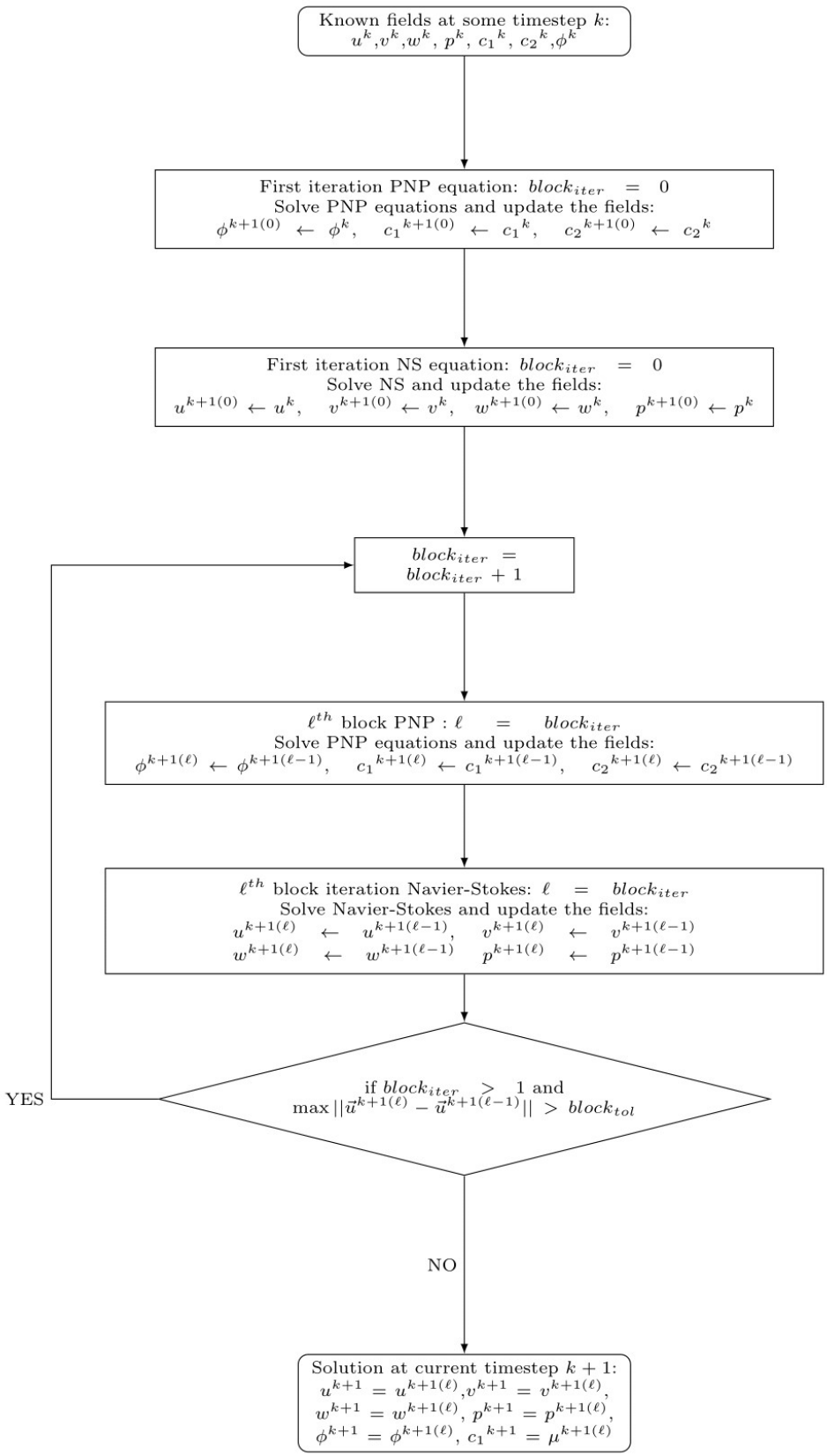


**Figure S10**. Flowchart for NS-PNP Block Algorithm for a given timestep.

**Figure S11** shows the distribution of ionic strength obtained in the simulation result. The ionic strength is near to that of the bulk fluid at the upstream boundary of the simulated domain and transitions abruptly to an IDZ within approx. 100 $\mu$m of the planar electrode (**Figure S11a**). In the device with conductive microbeads, the vortices create inroads for cation transport to the electrode, which can be observed as narrow extensions of bulk ionic strength across the IDZ (**Figure S11b**). This enhanced mass transport is what facilitates direct transition from ohmic to overlimiting regimes.

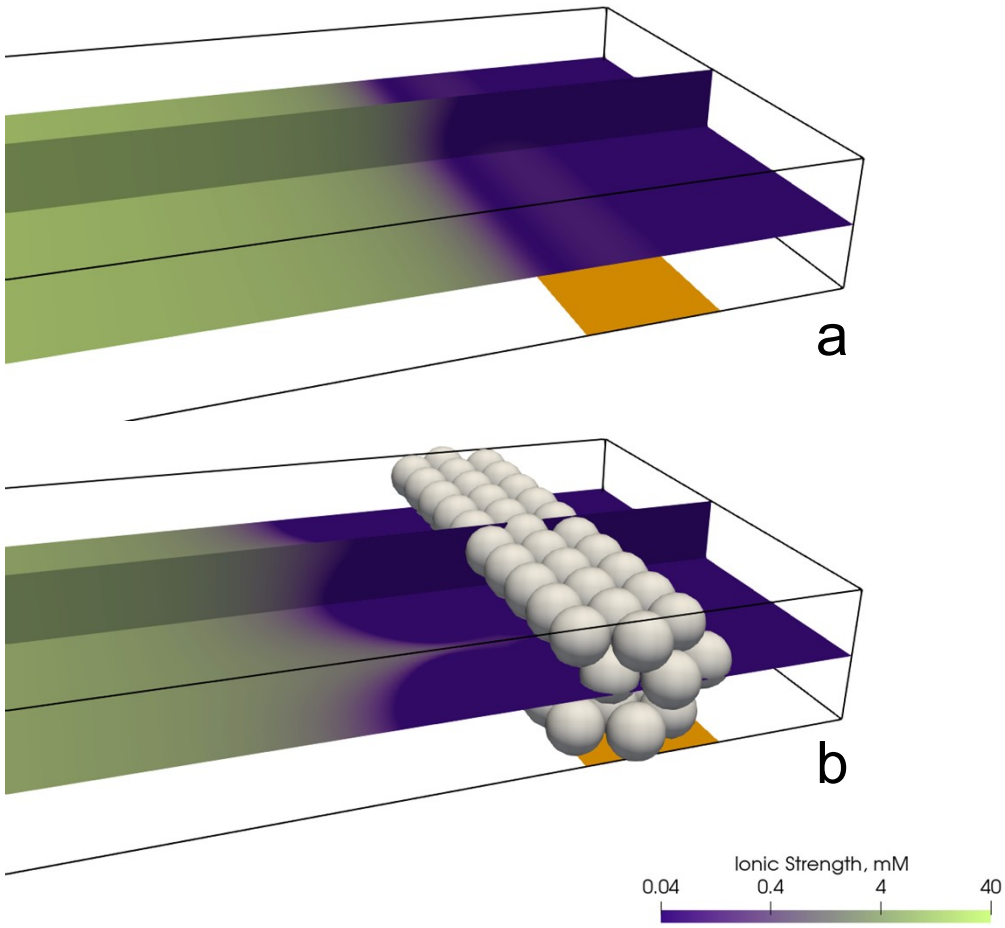


**Figure S11**. Surface plot of the simulated ionic strength in the (a) absence and (b) presence of conductive microbeads overlying the planar microband electrode. At this cathode, cations of the bulk electrolyte are consumed, leading to the formation of an IDZ. Panel (b) shows that the microbeads facilitate formation of vortices that drive mass transport of ions across the IDZ to the electrode surface.

**References**.


(1) McDonald, J. C.; Whitesides, G. M. Poly (Dimethylsiloxane) as a Material for Fabricating Microfluidic Devices. *Acc. Chem. Res.* **2002**, *35*, 491–499.

(2) Xia, Y.; Whitesides, G. M. Soft Lithography. *Annu. Rev. Mater. Sci.* **1998**, *28*, 153–184.

(3) Elgrishi, N.; Rountree, K. J.; McCarthy, B. D.; Rountree, E. S.; Eisenhart, T. T.; Dempsey, J. L. A Practical Beginner's Guide to Cyclic Voltammetry. *J. Chem. Educ.* **2018**, *95*, 197–206

(4) Kim, S.; Anand, R. K.; Ganapathysubramanian, B. Modeling Electrochemical Systems with Weakly Imposed Dirichlet Boundary Conditions. *Prepr. Submitt. to Elsevier* **2020**, 1–24.

(5) Ishii, M.; Fernando, M.; Saurabh, K.; Khara, B.; Ganapathysubramanian, B.; Sundar, H. Solving PDEs in Space-Time: 4D Tree-Based Adaptivity, Mesh-Free and Matrix-Free Approaches. *Int. Conf. High Perform. Comput. Networking, Storage Anal. SC* **2019**.

(6) Kumar, S.; Ishii, M.; Fernando, M.; Gao, B.; Tan, K.; Hsu, M.-C.; Krishnamurthy, A.; Sundar, H.; Ganapathysubramanian, B. Scalable adaptive PDE solvers in arbitrary domains. *arXiv preprint* **2021** *arXiv:2108.03757*.